A new damage evolution criterion for the coupled Eulerian-Lagrangian approach: Application to three-dimensional numerical simulation of segmented chip formation mechanisms in orthogonal cutting

D. Ambrosio [a*], A. Tongne [a], V. Wagner [a], G. Dessein[a], O. Cahuc [b]

[a] *Laboratoire Génie de Production, ENI Tarbes, 65016 Tarbes, France*

[b] *Université de Bordeaux, CNRS, ENSAM, I2M Bordeaux, 351 cours de la Libération, Talence, France*

Abstract

A damage evolution law is proposed to consider the frictional behavior within an Eulerian material after full damage as a Lagrangian material, where the mesh explicitly describes the newly born interface interactions. This approach is prominent for simulating severe plastic deformation (SPD) processes during which material separation can occur. Among these, orthogonal cutting represents the simplest process for comparison with the simulation because it offers accessibility for measuring physical quantities in situ in the vicinity of the tool. Therefore, a numerical model based on a coupled Eulerian-Lagrangian formulation to simulate segmented chip formation mechanisms during orthogonal cutting was developed. A simple damage initiation criterion was used, and the damage evolution criterion was coded in the ABAQUS subroutine VUSDFLD. The model can simulate both segmented and continuous chip formation, depending on the experimental configuration, while satisfactorily predicting chip morphology and physical quantities such as temperature, primary shear band and cutting forces. Additionally, a non-negligible material side flow observed experimentally was successfully predicted by simulation. The model accuracy in predicting the material plastic behavior is auspicious for its subsequent extension to the three-dimensional model of SPD processes (i.e., milling, friction stir welding, etc.).

Keywords: damage evolution, coupled eulerian-lagrangian (CEL), orthogonal cutting, segmented chip formation, frictional behavior

1 Introduction

The coupled Eulerian-Lagrangian (CEL) method based on the combination of Lagrangian and Eulerian formalisms has been recently applied to various manufacturing processes. Qiu et al. [1] highlighted the great advantage offered by the CEL approach in combining the benefits of both traditional formulations (i.e., Lagrangian and Eulerian) by defining an Eulerian workpiece and a Lagrangian tool that avoid contact and mesh distortion problems. Consequently, there is increasing interest in simulating severe plastic deformation

*Corresponding author

Email address: dambrosi@enit.fr (D. Ambrosio [a])

(SPD) processes using the CEL formulation. Abdelhafeez et al. [2] successfully simulated drilling of aluminum and titanium alloys, demonstrating the CEL model's higher computational efficiency and accuracy. With a CEL model, Wu et al. [3] investigated the evolution of dislocation density and grain size in orthogonal cutting of Al6061-T6 alloy using micro-grooved cemented carbide cutting tools. The complex friction stir welding process was also simulated using the CEL approach proposed by Tongne et al. [4]. These authors were able to describe the formation mechanisms of regular banded structures in a friction stir weld bead. However, in the CEL approach, friction within the workpiece resulting from damage to the newly born interfaces is neglected.

Recently, interest has also been directed toward the potential application of the CEL method to simulate orthogonal cutting. However, in machining processes, material separation can occur within the manufactured parts owing to damage [5]. The resulting new interfaces are not explicitly described in the Eulerian formulation as they are in the Lagrangian formulation, where the mesh can describe newly born interfaces [6]. Therefore, the interfacial friction that maintains the material resistance after full damage is not considered in the Eulerian formulation. In this study, we propose a new damage evolution law that considers the friction at the interface after full damage. By considering that frictional behavior is at the origin of segmented chip formation, this approach is applied to orthogonal cutting. Its advantage over other processes is the possibility of extensively comparing simulation and experiment with forces, temperatures, chip morphology, etc., which, in other processes, is more complicated to access and to follow the tool-workpiece contact zone to make comparisons [7]. It follows that, if it is possible to correctly simulate orthogonal cutting with this approach, predicting chip formation mechanisms and chip morphology, the approach and the material behavior laws can then be extended to other processes. Ducobu et al. [8] were the first to apply the CEL approach to orthogonal cutting successfully. The major outcome to assess the validity of their two-dimensional (2D) CEL model, based on the Johnson-Cook (JC) constitutive law, was the closeness between the results of the new and the traditional Arbitrary Lagrangian-Eulerian (ALE) and Lagrangian models. Subsequently, they extended the previous 2D model to achieve a three-dimensional (3D) simulation of orthogonal cutting, succeeding in predicting the lateral material flow during plastic deformation [9]. The first simulation using this approach reporting segmented chip prediction was presented by Shuang et al. [10]. Their 2D model was based on a modified JC law, but no damage law was included. The authors also did not compare the Ti6Al4V chip morphology obtained by simulation with experiments, except qualitatively. The first application of aluminum alloys was reported by Ducobu et al. [11]. Based on a JC law describing the material plastic behavior, the authors correctly simulated continuous chip formation employing Bao-Wierzbicki (B-W) [12] model for damage initiation. However, an average error of approximately 20% between the simulated and measured shear forces should be noted. Agmell et al. [13] first developed a 3D CEL model to simulate the

chip mechanism formation in AISI 316L. Based on the JC constitutive law, the simulation predicted the segmented chip, but an accurate comparison of chip morphology was not performed. The simulated and measured average forces are close to each other, although the oscillation resulting from chip formation is almost nonexistent in the measurements, but it is evident in the simulation. Therefore, it is understood that the model does not accurately simulate the experimental chip formation mechanism. Recently, Xu et al. [14] developed a 3D model based on a newly developed plastic behavior law capable of predicting both segmented chip formation and the existence of a material-side flow. The damage laws in all models introduced have been based on the JC law for the initiation and energy criteria for evolution. Determining the parameters for these criteria requires many tests to characterize the material behavior as a function of strain, strain rate, and temperature to build a constitutive model [15]. Moreover, although in mechanical testing one attempts to reproduce conditions developed during manufacturing processes, the thermo-mechanical conditions in some processes, such as machining and friction stir welding, are different from those encountered in conventional mechanical testing [16].

Reviewing the various works in the literature on orthogonal cutting simulation with the CEL approach, summarized in Table 1, to highlight the differences makes it clear that several elements need to be improved to increase the predictive ability of the models. Independent of the approach, none of the reviewed CEL

Table 1: Summary of the reviewed models, showing the main information, including material behavior laws and type of model (2D or 3D) schematically. Base material (BM), continuous (Cont.) and segmented (Seg.).

Author -	**BM** -	**Plastic behaviour**	**Damage initiation**	**Damage evolution**	**Model** -	**Chip type**
Ducobu et al [8]	Ti6Al4V	J-C	N/A	N/A	2D	Cont.
Ducobu et al. [9]	Ti6Al4V	J-C	N/A	N/A	3D	Cont.
Shuang et al. [10]	Ti6Al4V	J-C TANH	N/A	N/A	2D	Seg.
Ducobu et al. [11]	AA2024-T3	J-C	B-W	Energy	2D	Cont.
Agmell et al. [13]	AISI 316L	J-C	J-C	Energy	3D	Seg.
Xu et al. [14]	Ti6Al4V	Proposed	J-C	Energy	2D/3D	Seg.
This work	AA6082-T6 / AA7075-T6	J-C	**Proposed**	**Proposed**	3D	Both

models exhibited the ability to predict different chip formation mechanisms (continuous and segmented). Most of the models are based on the JC plastic law or its modified versions. Some contradictions can be seen. For example, Shuang et al. [10] can predict different forms of segmented chips with modified JC, whereas Xu et al. [14] states that the JC constitutive law cannot successfully predict segmented chip mechanisms. At the same time, the only work demonstrating remarkable differences in the simulated chips is that of Shuang et al. [10], in which the damage law was not reported. Therefore, it is clear that several incongruities can be found in previous studies, confirming the need to improve existing models to predict chip formation mechanisms

using the CEL approach.

Therefore, in this work, a new damage evolution criterion is proposed to integrate the friction between the newly born surfaces in the workpiece when simulating 3D orthogonal cutting through the CEL method.

2 Modeling and simulation of orthogonal cutting

2.1 Description of the orthogonal cutting model

The 3D model is developed in the ABAQUS/Explicit framework. It is created using the CEL approach, which allows the modeling of a Lagrangian tool and an Eulerian workpiece. In this way, the workpiece material moves through fixed mesh elements according to the Eulerian formulation, overcoming the mesh distortion problem. The fixed Eulerian mesh domain is sufficiently large to cover the evolving workpiece geometry, especially chip formation. This ABAQUS/Explicit method is based on the volume of fluid method [17]. The Eulerian volume fraction for each Eulerian element is introduced. An element wholly filled with the material has a fraction equal to 1, whereas if no material is present, it is equal to 0. Therefore, the surrounding Eulerian volume at the beginning is empty, whereas the workpiece Eulerian volume is filled. Chip formation causes the empty elements to become either partially or completely filled with material during cutting. The Eulerian framework, workpiece and void, and Lagrangian tool in the initial condition are displayed in Fig. 1. The extent of this extra volume must contain the desired material flow. In this case, the height along the y

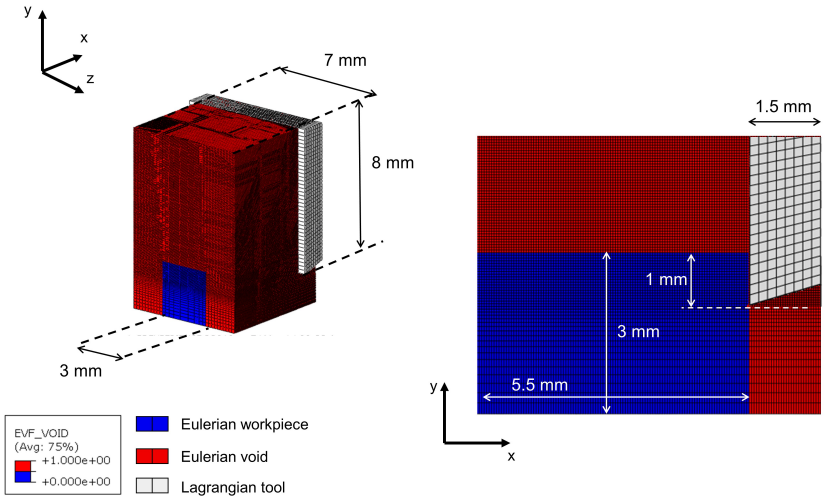

Figure 1: 3D orthogonal cutting model including Eulerian workpiece, Eulerian void, Lagrangian tool and dimensions.

direction is set to include at least three consecutive segmented chips in the various tests performed, and the depth in the z direction is defined to contain the observed lateral material flow.

The element type for the Eulerian medium, workpiece, and void is an eight-node thermo-mechanical coupled linear Eulerian brick element (EC3D8RT). A size of 5 microns in the cutting zone and an orientation of 90°

with respect to the cutting direction of the Eulerian parts are established based on [14] outcomes. The tool elements are eight-node linear thermo-mechanical coupled brick elements (C3D8RT).

The sketch of the boundary conditions is presented in Fig. 2 and facilitates the explanation. On the bottom surface, the displacements along y are blocked. A velocity along x equal to the cutting speed on the left surface is assigned, blocking the z direction to avoid material flow. The tool is fixed and modeled as a rigid body. The only initial condition set is the temperature, which is selected according to the type of test. The

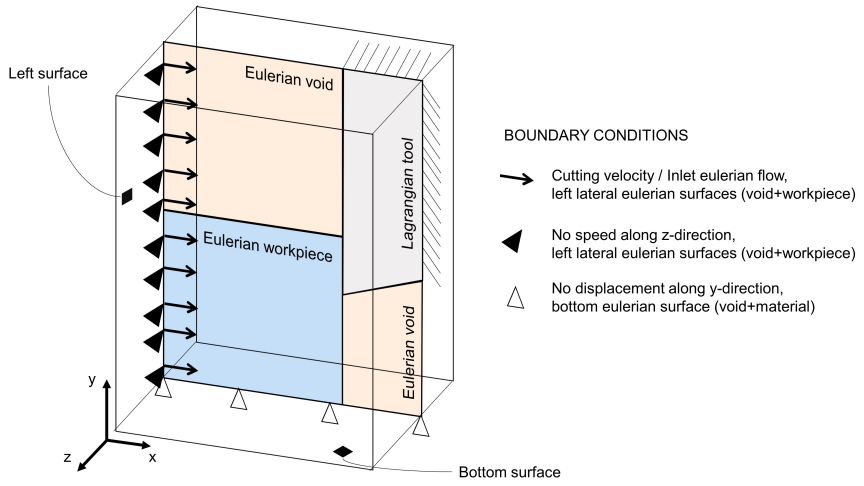

Figure 2: Boundary conditions.

tool-workpiece contact condition is modeled with Coulomb's law by setting a friction coefficient of 0.3 [18]. It is assumed that the heat generated by friction can be divided equally between the tool and workpiece [19] and that all the energy dissipated by the friction is converted into heat.

2.2 Constitutive law

2.2.1 Plastic behavior

The plasticity of the model is based on the widely used JC law (1), which describes the material behavior during plastic deformation, with temperature, strain, and strain rate all taken into account. The decision to use this law is made because of its wide use in the literature, allowing comparison of this model with other models.

$$\sigma = [A + B\varepsilon^n]\left[1 + C\ ln\frac{\dot{\varepsilon}}{\dot{\varepsilon_o}}\right]\left[1 - \left(\frac{T - T_o}{T_m - T_o}\right)^m\right] \tag{1}$$

The model parameters for the two materials AA6082-T6 [20] and AA7075-T6 [21] are taken from the literature and are listed in Table 2.

Table 2: Workpiece and tool material properties.

Base Material	A (MPa)	B (MPa)	C	n	m	$\dot{\varepsilon_o}$ $(s^{-}1)$	T_m (°C)
AA6082-T6	305	307	0.0044	0.68	1.31	1	582
AA7075-T6	473	210	0.033	0.38	1.5	1	635
Base Material	E (GPa)	ν	ρ (kg/m^3)	k (W/m°C)	c (J/kg°C)		
AA6082-T6	73	0.33	2700	170	960		
AA7075-T6	73	0.33	2700	130	900		
Steel tool	200	0.3	7800	N/A	N/A		

2.2.2 Damage initiation and evolution

The damage initiation is described using the traditional ductile criterion governed by state variable w:

$$w = \sum \frac{\Delta \bar{\varepsilon}^{pl}}{\bar{\varepsilon}_o^{pl}} \tag{2}$$

where $\Delta \bar{\varepsilon}^{pl}$ is the plastic strain increment and $\bar{\varepsilon}_o^{pl}$ is the plastic strain at the onset of damage. During deformation, the state variable w increases monotonically from 0 to 1 at the onset of damage. Even though $\bar{\varepsilon}_o^{pl}$ generally depends on the stress triaxiality and strain rate, it is assumed to be dependent only on the strain rate. Its calibration is made through experimental tests reproducing the experimental shear angles and chip segmentation frequencies. A piecewise linear function is proposed, as shown in Fig. 3 for the two materials.

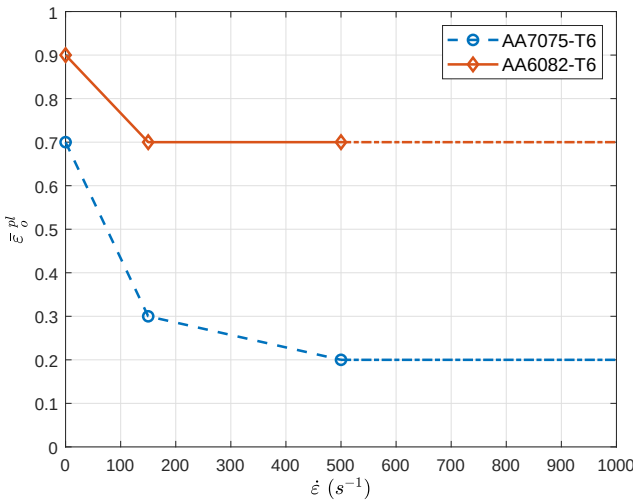

Figure 3: Equivalent plastic strain at damage initiation $\bar{\varepsilon}_o^{pl}$ as function of strain rate.

For damage evolution, instead of using the linear damage variable $D = \frac{\sum \Delta \bar{\varepsilon}^{pl}}{\bar{\varepsilon}_f^{pl}}$, the following multiplicative

function $f(\eta, T)$, which depends on the stress triaxiality η and temperature T, is proposed:

$$D = \frac{\sum \Delta \bar{\varepsilon}^{pl}}{\bar{\varepsilon}_f^{pl}} f(\eta, T) \tag{3}$$

where $\bar{\varepsilon}_f^{pl}$ is the plastic strain at failure, which depends on the characteristic length L_c of the element. Therefore, the material damage evolution properties are expressed in terms of the displacement at failure, $u_f = \dfrac{\bar{\varepsilon}_f^{pl}}{L_c}$. Before expressing $f(\eta, T)$, it is important to describe the proposed approach. First, it is noteworthy that the stress triaxiality η is equal to -0.33 for uniaxial compression, 0.33 for uniaxial tension, 0 for pure shear and $-\infty$ for hydrostatic pressure. The stress triaxiality can be expressed as

$$\eta = \frac{\sigma_m}{\bar{\sigma}} \quad \begin{cases} \sigma_m = (\sigma_1 + \sigma_2 + \sigma_3)/3 \\ \bar{\sigma} = \sqrt{\frac{1}{2}\left[(\sigma_1 - \sigma_2)^2 + (\sigma_2 - \sigma_3)^2 + (\sigma_3 - \sigma_1)^2\right]} \end{cases} \tag{4}$$

where σ_m is the hydrostatic pressure and $\bar{\sigma}$ is the von Mises equivalent stress. The expression for $f(\eta, T)$ is given by

$$f(\eta, T) = (c_1 - c_2)\,\frac{\eta_{max}(T) - \eta}{c_\eta} + c_2 \tag{5}$$

$$c_\eta = \eta_{max}(T) - \eta_{min}(T) \tag{6}$$

and c_1 and c_2 are the extreme values of D for the full and zero frictional effects, and they are fixed at 0.4 and 0.95, respectively. The goal of the proposed damage evolution law is to add additional resistance to the damaged material to the frictional interface. This is needed because, during damage, the material better resists compression than tension. By defining a temperature-dependent parameter, $\eta_{max}(T)$, the frictional interface is considered. Stress triaxiality equal to or lower than η_{min} leads to full frictional behavior, whereas if it is greater than or equal to η_{max}, there is no friction, as displayed in Fig. 4a. By assuming that the stress triaxiality is constrained within uniaxial compression ($\eta = -0.33$) and uniaxial tension ($\eta = +0.33$), a transition zone $c_\eta = 0.66$ is imposed for the material behavior description. Then, by integrating the η_{max} dependency on the element temperature, as schematically represented in Fig. 4b, thermal softening is taken into account and differences in the frictional behavior are considered. The $\eta_{max}(T)$ parameter dependency

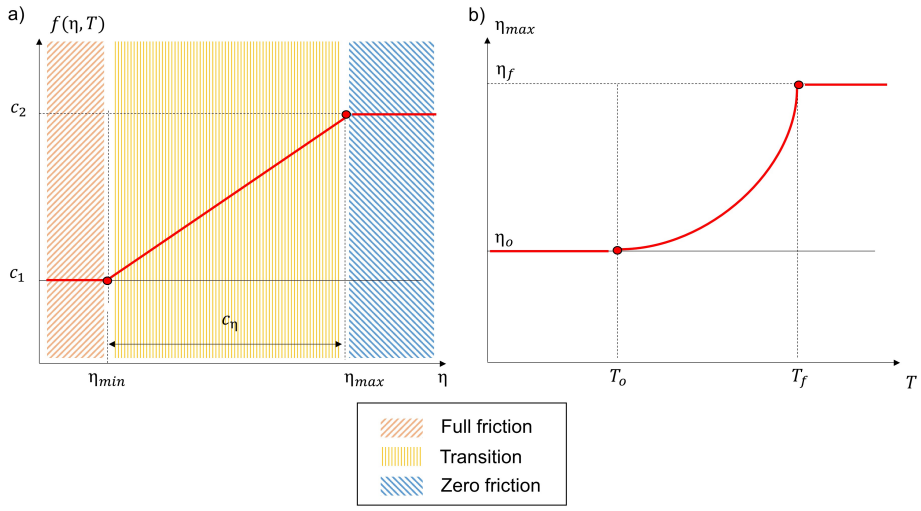

Figure 4: Conceptual dependencies representation of a) $f(\eta, T)$ on stress triaxiality and b) η_{max} on temperature.

on temperature is as follows:

$$\eta_{max}(T) = \begin{cases} \eta_0 & \text{if } T < T_0 \\ (\eta_f - \eta_0)\left(\frac{T-T_o}{T_f-T_o}\right)^{m_c} + \eta_0 & \text{if } T_0 \leq T \leq T_f \\ \eta_f & \text{if } T \geq T_f \end{cases} \tag{7}$$

where T_0 is room temperature, while T_f is the critical temperature when the aluminum alloys lose their strength due to microstructural modifications. The parameter tuning of the chip formation mechanism is η_{max}. Therefore, its limits for both materials, η_0 and η_f, as well as the temperature dependency, are inversely calibrated to reproduce the chip formation mechanism obtained experimentally. The function $f(\eta, T)$ is programmed in the ABAQUS subroutine VUSDFLD and is called the field variable in the tabular damage evolution law environment.

Therefore all the elements introduced in the model are following. At damage initiation, the equivalent plastic strain depends linearly on the strain rate and acts directly on the shear angle. Once the damage has started, the interaction at the interface is described by equation (3), which influences the chip separation mechanism. The novel separation criterion integrating the friction between the newly formed surfaces allows the simulation of chip formation mechanisms using the CEL approach. In the first subsection of the *Results and discussion* section, the calibration process is explained by illustrating how the temperature dependence of η_{max} (equation 7) is derived, and the results of the simulations performed once all dependencies are defined then discussed in the rest of the section.

3 Experimental setup

Tests are performed on a SOMAB Genymab 900 multitasking lathe (max cutting speed 30 m/min and max cutting force 10 kN), and four different configurations are tested on 3-mm-thick AA6082-T6 and AA7075-T6 sheets. The depth of cut is kept constant at 1 mm and the rake angle is set at 0°, while the other parameters are summarized in Table 3. Two tests for each configuration are performed, one with a high-speed camera

Table 3: Orthogonal cutting parameters.

BM -	$\mathbf{V}_c$ (m/min)	T_{start} (°C)
AA6082-T6	7.2	25
		180
	21	25
		180
AA7075-T6	7.2	25
		180
	21	25
		180

(HSC) and another with an infrared (IR) camera, while forces are always recorded with a Kistler 9129AA loadcell at 1500 Hz. The experimental setup is shown in Fig. 5, with details on the tool and the force and video acquisition system.

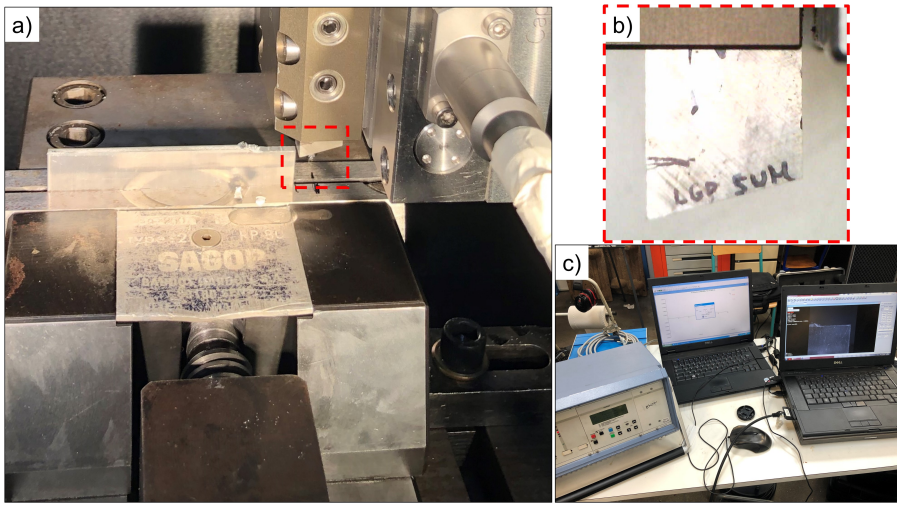

Figure 5: Experimental setup a) Lathe machine, b) tool detail, c) acquisition systems (forces and high speed cameras).

A sketch of the experimental setup and HSC and IR images (post-processed with MATLAB) are presented in Fig. 6. The HSC images are used to measure the primary shear angle, while the mean temperature in the

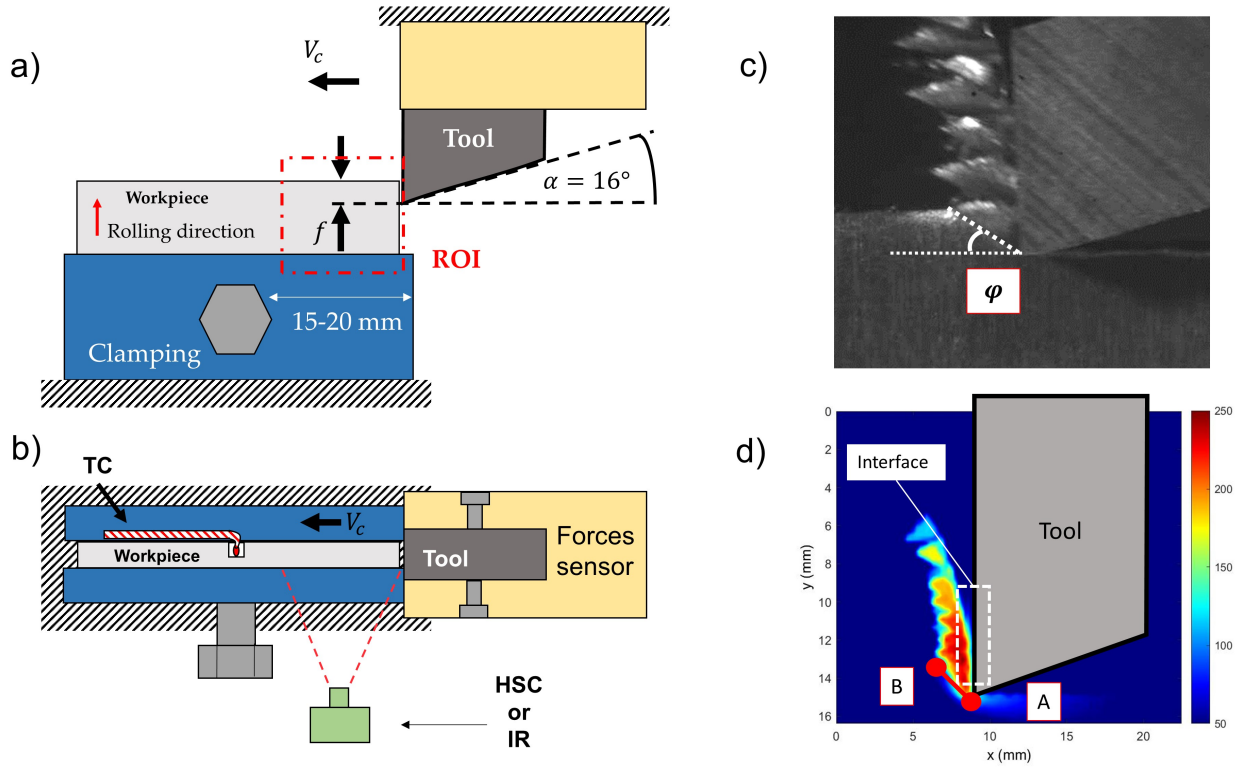

Figure 6: Sketch experimental setup a) front and b) top view. Frame from c) HSC and d) IR (after post-treatment).

primary shear plane and the maximum temperature in the secondary shear plane are determined using IR camera images. Local heating of the plates is performed using a blowtorch. The machined parts are black-painted to control the emissivity of the aluminum alloys, and the emissivity is calibrated using preliminary tests. In addition, in all high-temperature tests, to check that the information provided by the IR camera is correct, a thermocouple is inserted into the back of the plates, as shown in Fig. 6b. Additional information about the sensors (HSC and IR) is presented in the Appendix.

For chip preparation, the samples are polished down to $1/4$ μm, and AA7075-T6 chips are chemically etched by exposure to Keller's reagent to reveal the grains. The etched samples are inspected using an optical microscope (Olympus PMG3), while the other observations were are using a Keyence VHX6000 microscope. Changes caused by different test conditions, at room temperature or preheating, were investigated with Vickers hardness measurements. They are made on polished samples using a Zwick ZHU 2,5 durometer with a load of 4.9 N and a duration time of 10 s. Three indentations are performed in each different zone that makes up the chip.

4 Results and discussion

4.1 Influence of the damage variable on chip formation mechanism

The novelty introduced in this study is related to the damage evolution criterion. It depends on the stress triaxiality and coefficient η_{max}, the latter of which directly affects the stiffness degradation in the shear band. In the calibration phase of the model, this parameter is changed manually to act on the formed chip geometry in the various tests performed on the different materials. Fig. 7 shows the results three types of chips obtained under the same conditions (cutting speed, depth of cut, and initial temperature) and material properties by changing the value of η_{max}. Decreasing η_{max} results in D approaching 0.95, resulting in a

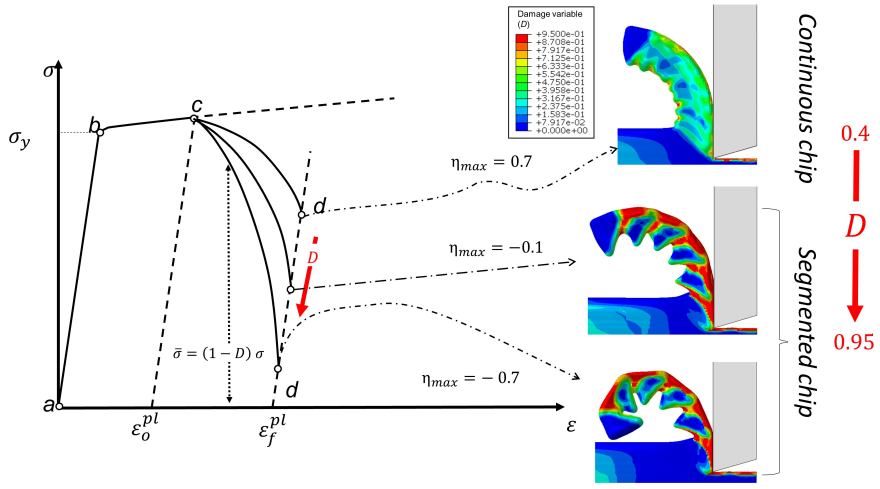

Figure 7: Stress-strain curve in the chip formation. a) Begin elastic deformation, b) yield point, c) damage initiation $w = 1$ and $D = 0$, d) material stiffness degradation limit (ε_f^{pl}). Influence of η_{max} on the chip formation mechanism

greater stiffness degradation in the shear band and, therefore, great separation between chips (zero friction). Choosing positive values of η_{max}, in contrast, results in D approaching the lowest values allowed with a reduction in the degradation in the shear band, favoring cohesion between successive chips and resulting in a continuous chip (full friction). Fig. 8a displays the element tracked during simulation to follow von Mises stress and damage variable evolution depending on η_{max}. Modifying the coefficient affects the element stiffness degradation reached cyclically in the shear band and, as a consequence, as damage is initiated, the von Mises stress evolution changes, as displayed in Fig. 8b.

In the experiments, a continuous chip is obtained only in the hot configurations of alloy AA7075-T6. By analyzing the chip transversal microstructure and the hardness in the various areas that make up the chip, the difference between the two tests at room temperature and with pre-heating is evident, as displayed in Fig. 9. The microstructure obtained at room temperature (Fig. 9b) is similar to those of the base material (Fig. 9a) but deformed by shear. However, in the test with pre-heated plates, the microstructure begins to

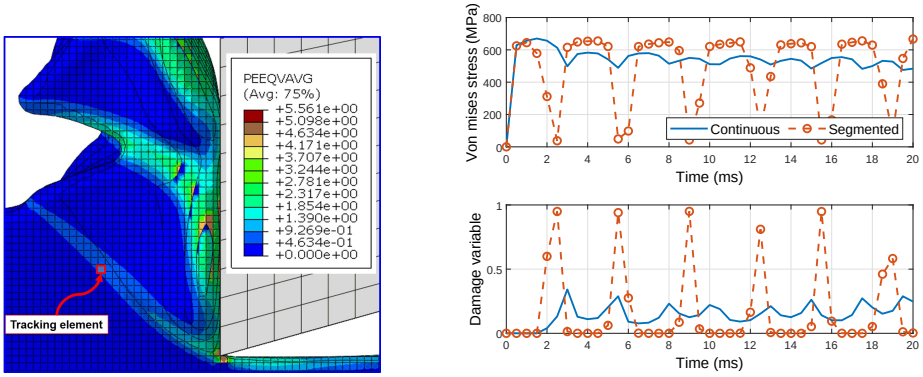

(a) Tracked element.

(b) Von mises stress and damage variable evolution in the tracked elements.

Figure 8: Influence of η_{max} on the simulation. Continuous η_{max}= 0.7, segmented η_{max}= -0.7.

have characteristics different from those of the base materials, such as various grains with different shapes, sizes, and orientations (Fig. 9c). The different microstructures are due to dynamic recovery, which is the governing softening mechanism during hot deformation of AA7075-T6 at high temperatures up to $350°C$ [22]. Furthermore, the measured hardness decreases dramatically in the hot configuration owing to the gradual transformation of the strengthening precipitates (Fig. 9d). As a result, a continuous chip is obtained instead of a segmented chip (Fig. 10).

Hence, based on the experiments and literature, η_{max} coefficient is made temperature-dependent. The high mechanical strength of aluminum alloys in the T6 state is due to the high density of strengthening precipitates induced by heat treatments [23]. However, once certain temperatures are reached, these precipitates begin to progressively grow, losing their strengthening effect and causing a drastic decrease in the material's mechanical strength [24] because of dynamic recovery and dynamic recrystallization. The critical temperatures in the two materials are different, and, based on previous studies, are fixed between $250 - 350°C$ for AA6082-T6 [25] and between $200 - 300°C$ for AA7075-T6 [26]. Consequently, the η_{max} parameter changes within the ranges until the critical temperature T_f is reached, as shown in Fig. 11. The values attributed to the model parameters are listed in Table 4.

Table 4: Damage constitutive model parameters for the two materials.

BM	c_1	c_2	c_η	η_f	η_0	m_c	T_f
AA6082-T6	0.4	0.95	0.66	0.7	-0.2	2	$350°C$
AA7075-T6	0.4	0.95	0.66	0.7	-0.3	7	$300°C$

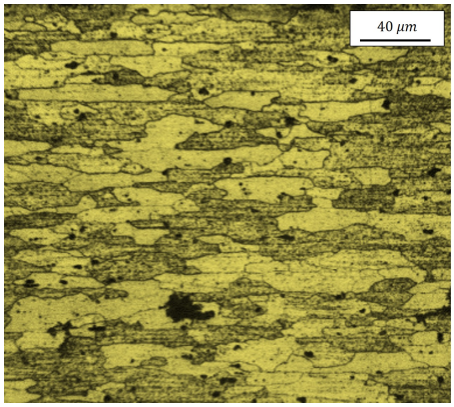

(a) AA7075-T6 - Base material.

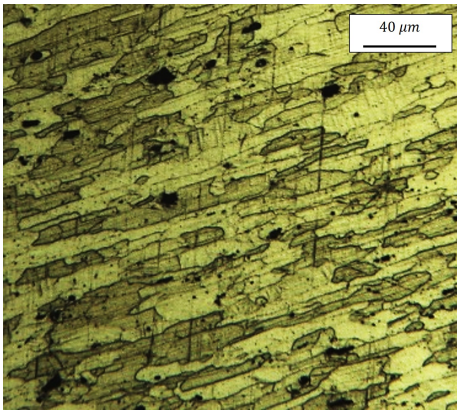

(b) AA7075-T6 - Room temperature

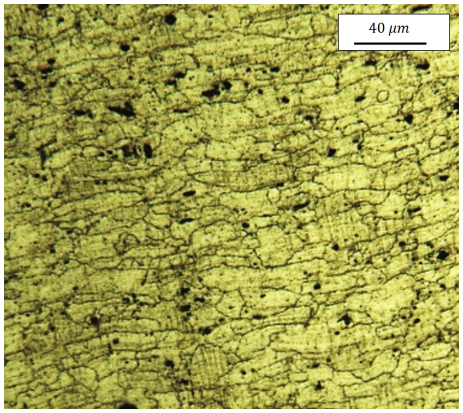

(c) AA7075-T6 - Pre-heated

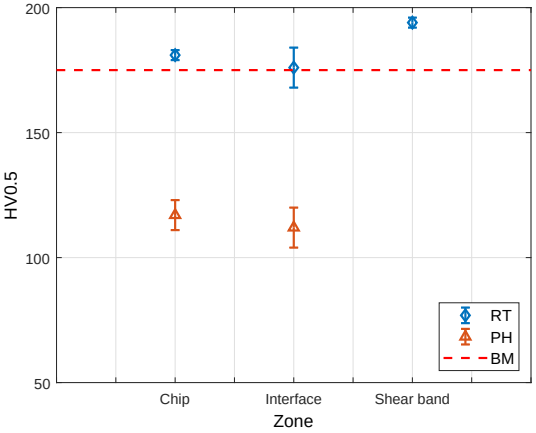

(d) Hardness measurements

Figure 9: Microstructure of the base material and the chip obtained in configuration at room temperature and pre-heated and hardness in the chip different zones.

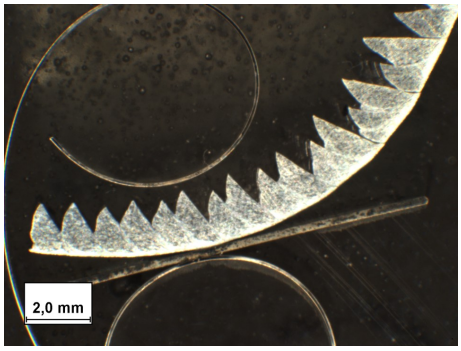

(a) Room temperature .

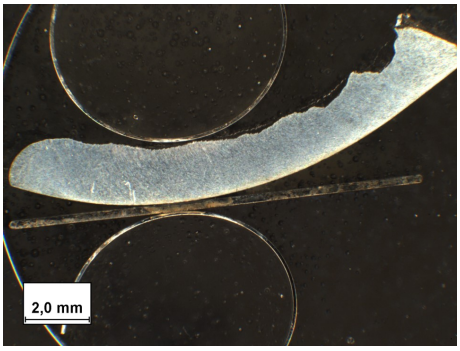

(b) Pre-heated.

Figure 10: Segmented and continuous chips obtained in the tests at 21 m/min on AA7075-T6.

4.2 Comparison between measured and simulated physical quantities

The cutting force and temperature are monitored during the tests. Fig. 12 shows a comparison of the force evolution over time in different configurations. The cutting force evolution is predicted with a good

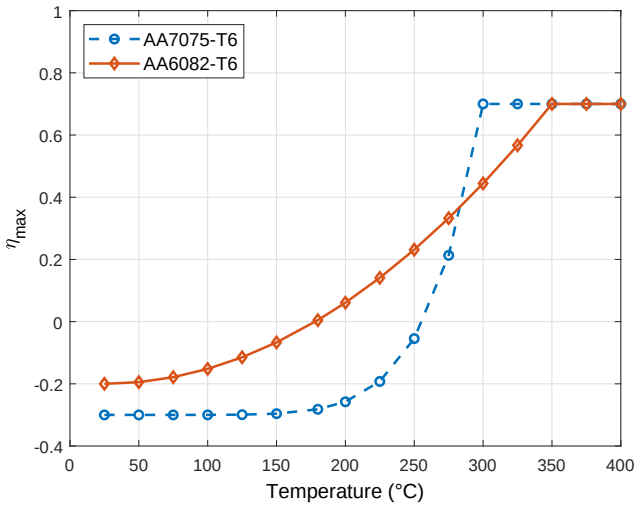

Figure 11: Evolution of η_{max} as function of the temperature.

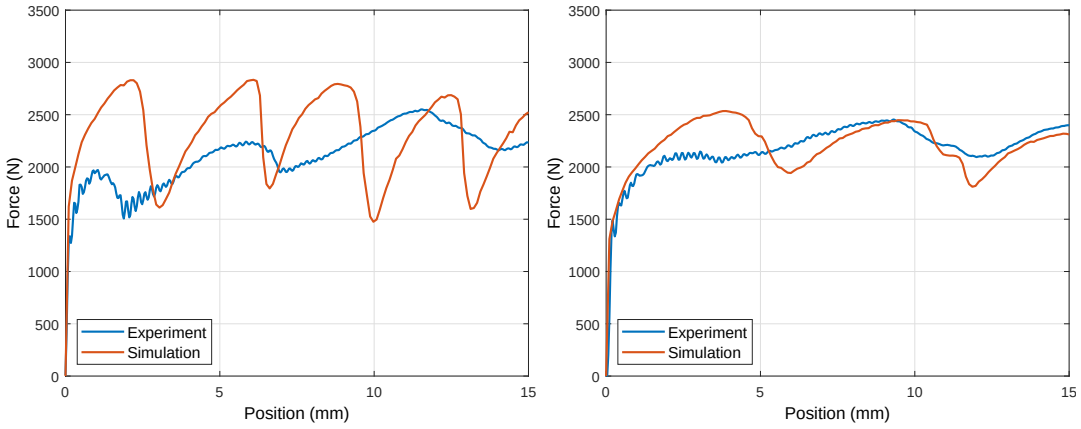

(a) AA6082-T6 - Room temperature.

(b) AA6082-T6 - Pre-heated.

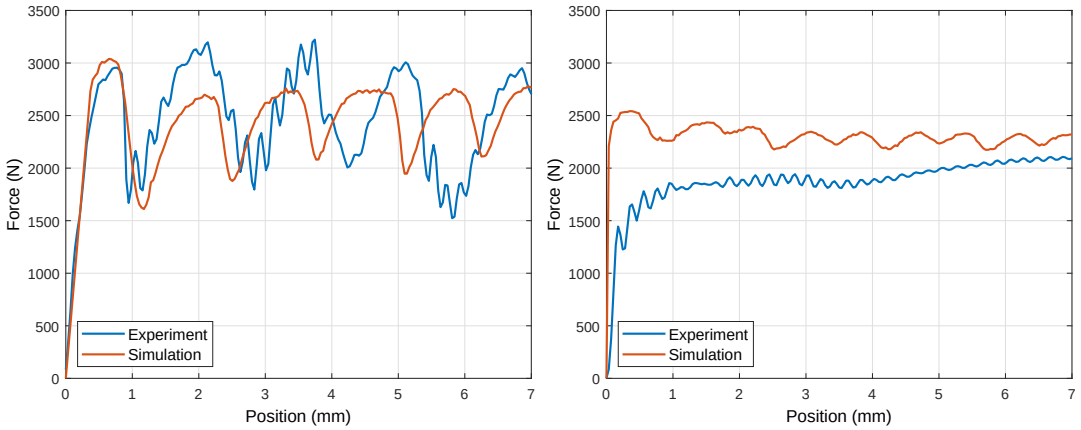

(c) AA7075-T6 - Room temperature.

(d) AA7075-T6 - Pre-heated.

Figure 12: Forces evolution during the formation of at least three consecutive chips in all tests performed at 21 m/min.

approximation by the model. The model consistently reproduces the observed experimental oscillation that coincides with chip formation. It is noteworthy that the model can capture the differences in the periodicity of the forces depending on the test. However, some differences are observed, and these are related to experimental inaccuracies. In Fig. 12a, the experimental first peak is lower than the simulated one, but this difference is associated with the slight inaccuracy of the depth of cut during the AA6082-T6 tests owing to the deformation caused by the previous pass. In contrast, in the hot test (Fig. 12d), in the simulation, a homogeneous temperature is predefined throughout the piece, but during experiments the heating is local at the first contact points with the tool. Therefore, at these points, the temperature may have exceeded the preset temperature of 180 °C or in any case the exposure to these high temperatures induced an excessive decrease in the resistance of the material. However, once the first few millimeters are advanced, the forces begin to approach each other. Fig. 13a shows the mean values of all forces with their standard deviations. Overall, the prediction of the model is reliable, with an error that is always below 10%. Similarly, the ability

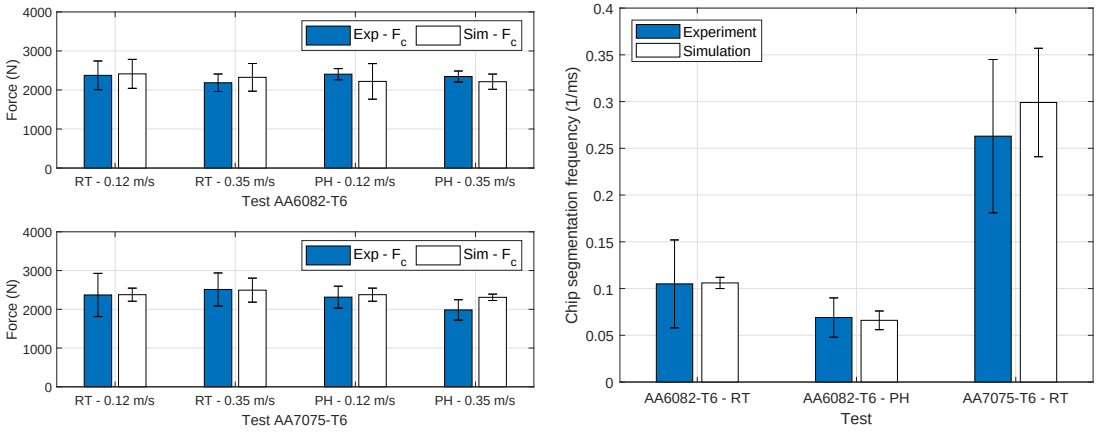

(a) Average values and standard deviation of cutting forces.

(b) Chips segmentation frequency at 21 m/min.

Figure 13: Comparison between experiment and simulation of cutting forces and chip segmentation frequency.

of the model to predict the chip segmentation frequency is accurate, as shown in Fig. 13b, where the simulated average time to chip creation in the 21 m/min configurations agrees with the experimental results.

With respect to the temperature, as observed from the thermal field obtained through the numerical simulation displayed in Fig. 14, the temperature rise resulting from plastic deformation is always higher in AA7075-T6 than in AA6082-T6. The temperature measurements with the IR camera allow estimating the average temperature in the primary shear zone by averaging the temperature in the pixels along with AB, as displayed in Fig. 6d. Similarly, the maximum temperature at the interface with the tool is estimated by averaging the maximum values among the pixels in the white dashed rectangle recorded in each image (Fig. 6d). The same is done in the simulations, and the comparison for all configurations is shown in Fig.

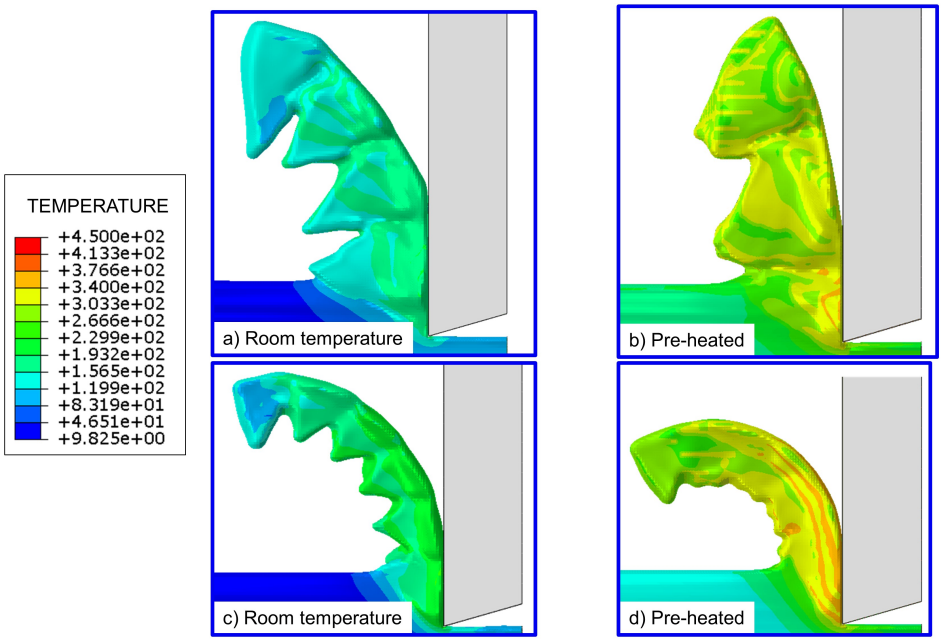

Figure 14: Thermal field in different configurations: a), b) AA6082-T6 and c), d) AA7075-T6.

15. A comparison between the measured and simulated values confirms the quality of the model's prediction

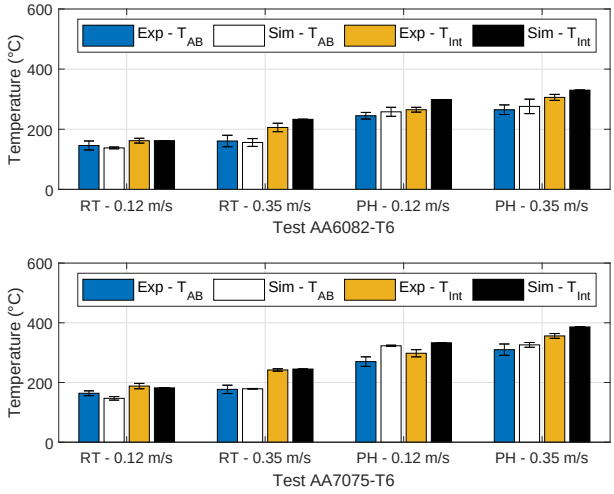

Figure 15: Thermal field for room temperature (RT) and pre-heated (PH) configurations both materials.

and its ability to describe heat generation resulting from tool-workpiece interaction. Therefore, the model reliability in predicting the thermo-mechanical quantities developed during the process, such as forces and temperatures, is demonstrated.

4.3 Chip morphology

The goal of introducing the new damage evolution criterion is to predict the type of chip formation mechanism, depending on the cutting conditions. We also aim to get as close as possible to the experiments in

terms of chip morphology. The results obtained shown in Fig. 16 demonstrate the achievement of both set

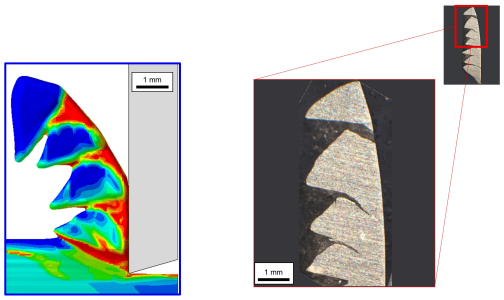

(a) AA6082-T6 - Room temperature.

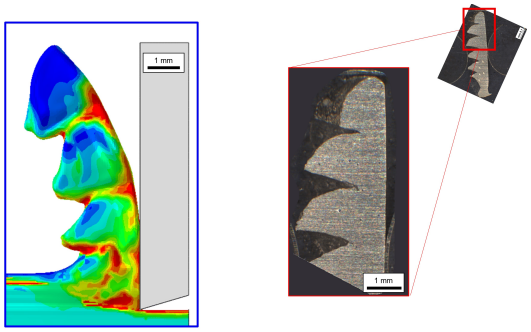

(b) AA6082-T6 - Pre-heated.

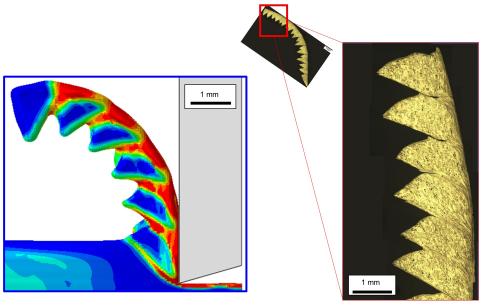

(c) AA7075-T6 - Room temperature.

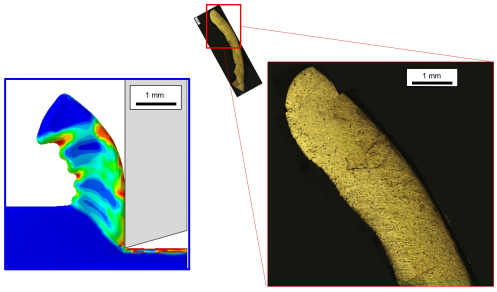

(d) AA7075-T6 - Pre-heated.

Figure 16: Comparison between chip obtained experimentally and numerically.

goals. The model correctly predict both chip formation mechanisms. In addition, qualitatively, good similarity between the numerical and experimental results can be observed. The geometries of the experimental and simulated chips are evaluated by calculating their peaks, valleys, chip widths, and shear angles. The various quantities are shown in Fig. 17. The geometric values are presented in Table 5, with a focus on configura-

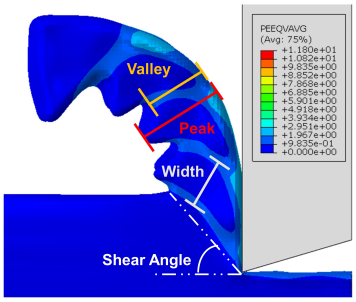

(a) Simulated chip showing peak, valley, width and shear angle.

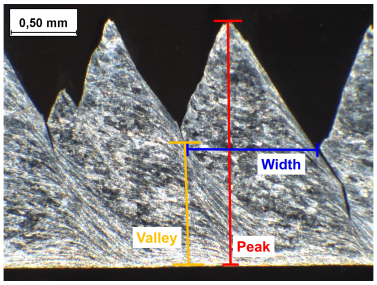

(b) Chip obtained from experiment showing peak, valley and width.

Figure 17: Identification of chip geometry characteristics.

220

tions at 21 m/min in which a segmented chip is obtained. The percentage errors are approximately around

Table 5: Chips geometry.

BM	Config.	Peak	Valley	Witdh	Shear angle
AA6082-T6 - RT	Exp.	2.55 ± 0.19	0.78 ± 0.27	1.59 ± 0.42	26
	Sim.	2.34 ± 7.2	1.05 ± 0.06	1.50 ± 0.07	30
	absolute err.	9%	25%	6%	13%
AA6082-T6 - PH	Exp.	2.73 ± 0.10	1.13 ± 0.21	1.65 ± 7.2	20
	Sim.	2.4 ± 0.01	1.31 ± 0.02	2.02 ± 0.18	24
	absolute err.	13%	13%	18%	16%
AA7075-T6 - RT	Exp.	1.64 ± 0.07	0.76 ± 0.17	0.98 ± 0.07	33
	Sim.	1.35 ± 0.05	0.65 ± 0.05	1.03 ± 0.07	30
	absolute err.	21%	15%	5%	10%

10% (except for a few cases in which it exceeded 20%), confirming the overall good predictive quality of the simulation in capturing complex phenomena such as the cyclic formation of shear bands and the formation of chips during orthogonal cutting.

Regardless of what occurs in the cutting plane, a remarkable material side flow for both aluminum alloys occurred during the experiments. Similarly, an out-of-plane deformation is observed in the simulation. Therefore, the chip thicknesses obtained experimentally and by simulation are compared for the configuration at room temperature and 21 m/min for both materials, as shown in Fig. 18. The simulation proved capable of predicting the material side flow well with an error of 2% and 8% for AA7075-T6 and AA6082-T6, respectively. From a qualitative point of view, by observing both the front and back of the chip in the two configurations, the results obtained with the simulation can be considered successful. This result is important, especially regarding the frequent assumption made in many simulations of the orthogonal cutting process in which it is considered a 2D process [27]. It is evident that, in the case of aluminum alloys, the deformation out of the plane is significant and could probably be detrimental to the application of digital image correlation technique measure the strain and strain rate gradient in shear zones. For AA7075-T6 [28] and Ti6Al4V [29], the digital image correlation technique is successfully applied for 0.25-mm-depth of cuts. However, if higher depths of cuts are used, the out-of-plane strain can be problematic for strain measurements through digital image correlation, leading to poor image sharpness and unsuccessful measurement owing to the material side flow [30].

5 Conclusion

A 3D numerical simulation of orthogonal cutting with a CEL approach based on a new inversely calibrated damage evolution criterion is proposed. The damage evolution function is developed and calibrated on tests with AA6082-T6 and AA7075-T6 under different experimental conditions, replacing the laborious

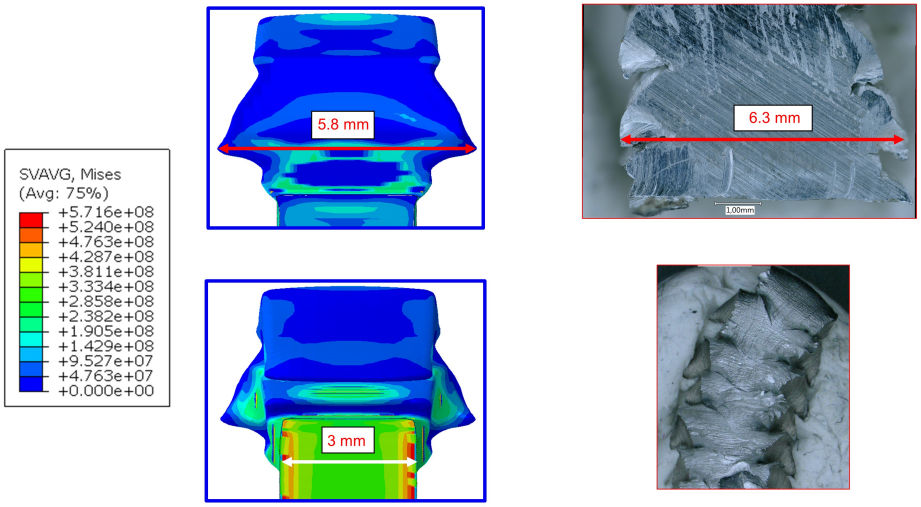

(a) Back and frontal view of AA6082-T6 chip obtained experimentally and numerically.

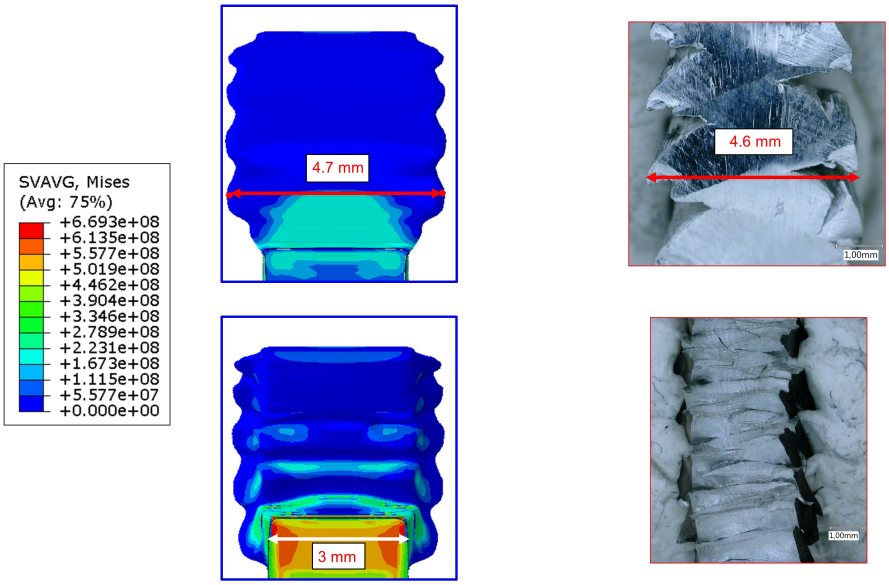

(b) Back and frontal view of AA7075-T6 chip obtained experimentally and numerically.

Figure 18: Comparison between chip thickness after cutting at 21 m/min at room temperature due to material side flow.

and complex material testing required to develop constitutive equations. With the new approach, integrating the friction between newly formed surfaces during cutting, the changes induced by experimental conditions resulting in different interactions between consecutive chips (and different mechanisms, from severely segmented to continuous chips) are correctly reproduced. At the same time, the simulation does not suffer a loss in quality in predicting the physical quantities generated during the process and can also capture the out-of-plane deformations that occur during orthogonal cutting. Moreover, the simulation can correctly capture

the material behavior of the processed part from its elastic response to the degradation induced by damage initiation and propagation. This result is auspicious for extending the new damage evolution criterion by considering the friction within the Eulerian workpiece in severe deformation processes simulated through the CEL approach.

CRediT authorship contribution statement

Danilo Ambrosio: Conceptualization, Methodology, Validation, Formal analysis, Investigation, Data Curation, Writing - Original Draft, Writing - Review and Editing, Visualization. **Amevi Tongne**: Conceptualization, Methodology, Formal analysis, Writing - Review and Editing. **Vincent Wagner**: Formal analysis, Investigation, Writing - Review and Editing. **Gilles Dessein**: Formal analysis, Investigation, Writing - Review and Editing, Resources, Supervision, Project administration. **Olivier Cahuc**: Resources, Writing - Review and Editing, Supervision, Project administration, Funding acquisition.

Acknowledgements

The authors want to thank Leo Bellon for the execution of orthogonal cutting tests.

Funding

This work was supported by the European Union's Marie Skodowska-Curie Actions (MSCA) Innovative Training Networks (ITN) H2020-MSCA-ITN-2017 under the grant agreement N°764979.

Data Availability

The raw/processed data required to reproduce these findings cannot be shared at this time due to technical or time limitations.

References

[1] Qiu G, Henke S, Grabe J. Application of a Coupled Eulerian-Lagrangian approach on geomechanical problems involving large deformations. Computers and Geotechnics 2011;38(1):30-39.

[2] Abdelhafeez AM, Soo SL, Aspinwall D, Dowson A, Arnold D. A Coupled Eulerian Lagrangian Finite Element Model of Drilling Titanium and Aluminium Alloys. SAE International Journal of Aerospace 2016;9(1):198-207.

[3] Wu H, Ma J, Lei S. FEM prediction of dislocation density and grain size evolution in high-speed machining of Al6061-T6 alloy using microgrooved cutting tools. Int. J. Adv. Manuf. Technol. 2018;95, 4211-4227.

[4] Tongne A, Desrayaud C, Jahazi M, Feulvarch E. On material flow in Friction Stir Welded Al alloys, J Mater Process Technol 2017;239:284-296.

[5] Vaziri M R, Salimi M, Mashayekhi M. Evaluation of chip formation simulation models for material separation in the presence of damage models, Simul Model Pract Theory 2011;19, 718-733

[6] Rodriguez J M, Carbonell J M, Jonsń P. Numerical Methods for the Modelling of Chip Formation. Arch. Comput. Methods Eng. 2020;27, 387-412.

[7] Boldyrev I S. EFG-simulation of the free orthogonal cutting and cutting forces prediction. Procedia Engineering 2017;206, 1201-1204 .

[8] Ducobu F, Riviére-Lorphévre E, Filippi E. Application of the Coupled Eulerian-Lagrangian (CEL) method to the modeling of orthogonal cutting. Eur J Mech A Solids 2016, 59:58-66.

[9] Ducobu F, Riviére-Lorphévre E, Filippi E. Finite element modelling of 3D orthogonal cutting 295 experimental tests with the Coupled Eulerian-Lagrangian (CEL) formulation. Finite Elem Anal Des 2017;134:27-40.

[10] Shuang F and Chen X, Ma W. Numerical analysis of chip formation mechanisms in orthogonal cutting of Ti6Al4V alloy based on a CEL model. Int. J. Mater. Form. 2018; 11,185-198.

[11] Ducobu F, Riviére-Lorphévre E, Galindo-Fernandez M, Ayvar-Soberanis S, Arrazola P J, Ghadbeigi H. Coupled Eulerian-Lagrangian (CEL) simulation for modelling of chip formation in 300 AA2024-T3. Procedia CIRP 2019;82:142-147.

[12] Bao Y and Wierzbicki T. On fracture locus in the equivalent strain and stress triaxiality space. Int. J. Mech. Sci 2004; 46(1):81-98.

[13] Agmell M, Bushlya V, Laakso S V, Ahadi A, Ståhl J E. Development of a simulation model tostudy tool loads in pcBN when machining AISI 316L. Int. J. Adv. Manuf. Technol. 2018; 96(5-8):2853-2865.

[14] Xu X, Outeiro J, Zhang J, Xu B, Zhao W, Astakhov V. Machining simulation of Ti6Al4V using coupled Eulerian-Lagrangian approach and a constitutive model considering the state of stress. Simul Model Pract Theory 2021.

[15] Cheng W, Outeiro J, Costes J P, M'Saoubi R, Karaouni H, Astakhov V. A constitutive model for Ti6Al4V considering the state of stress and strain rate effects. Mech. Mater. 2019;137-285.

[16] Iturbe A, Giraud E, Hormaetxe E, Garay A, Germain G, Ostolaza K, Arrazola P J. Mechanical characterization and modelling of Inconel 718 material behavior for machining process assessment. Mater. Sci. Eng. A 2017;441-453, 2017.

[17] Abaqus. Abaqus 6.10 user's manual, eulerian analysis.

[18] Melkote S N, Grzesik W, Outeiro J, Rech J, Schulze V, Attia H, Arrazola P J, M'Saoubi R, Saldana C. Advances in material and friction data for modelling of metal machining. CIRP Annals - Manufacturing Technology 2017;66(2):731-754.

[19] Rech J, Arrazola P J, Claudin C, Courbon C, Pusavec F, Kopac J. Characterisation of friction and heat partition coefficients at the tool-work material interface in cutting. CIRP Annals - Manufacturing Technology 2013;62(1):79-82, 2013.

[20] Chen X, Peng Y, Peng S, Yao S, Chen C, Xu P. Flow and fracture behavior of aluminum alloy 6082-T6 at different tensile strain rates and triaxialities. PLoS ONE 2017;12(7):1-28.

[21] Zhang D N, Shangguan Q Q, Xie C J, Liu F. A modified Johnson-Cook model of dynamic tensile behaviors for 7075-T6 aluminum alloy. J. Alloys Compd. 2015; 619:186-194.

[22] Xiao W, Wang B, Wu Y, Yang X. Constitutive modeling of flow behavior and microstructure evolution of AA7075 in hot tensile deformation. Mater. Sci. Eng. A 2018;704-713.

[23] Gladman T. Precipitation hardening in metals. Materials Science and Technology 1999;15(1):30-36.

[24] Maisonnette D, Suery M, Nelias D, Chaudet P, Epicier T. Effects of heat treatments on the microstructure and mechanical properties of a 6061 aluminium alloy. Mater. Sci. Eng. A 2011;528(6):2718-2724.

[25] Xu Z, Ma H., Zhao N., Hu Z. Investigation on compressive formability and microstructure evolution of 6082-T6 aluminum alloy. Metals 2020;10(4).

[26] Dalai B, Moretti M A, Åkerström P, Arvieu C, Jacquin D Lindgren L.-E.. Mechanical Behavior and Microstructure Evolution During Deformation of AA7075-T651. Mater. Sci. Eng. A 2021.

[27] Calamaz M, Coupard D, Girot F. A new material model for 2D numerical simulation of serrated chip formation when machining titanium alloy Ti-6Al-4V. Int. J. Mach. Tools Manuf. 2008;48(3-4).

[28] Zhang D, Zhang X, Nie G, Yang Z, Ding H. Characterization of material strain thermal softening effects in the cutting process. Int. J. Mach. Tools Manuf. 2021;160:103672.

[29] Harzallah M, Pottier T, Senatore J, Mousseigne M, Germain G, Landon Y. Numerical and 305 experimental investigations of Ti-6Al-4V chip generation and thermo-mechanical couplings in orthogonal cutting. Int. J. Mech. Sci. 2017; 134:189-202.

[30] Zouabi H, Calamaz M, Wagner V, Cahuc O, Dessein G. Kinematic Fields Measurement during Orthogonal Cutting Using Digital Images Correlation: A Review. J. manuf. mater. process 2021;5(1):7.

Appendix A

Infrared camera

Calibration and data recording were managed by Altair software. The specifications for the measurements performed in room temperature and pre-heated tests are listed in Tab. 6 and Tab. 7, respectively.

Table 6: Characteristics and parameters IR camera for room temperature tests.

Thermal resolution	20 mK at 30 °C
Frequency	150 Hz
Type sensor	50 mm
Numerical resolution	320 x 256 pixels
Estimated spatial resolution	4.7 mm/pixel
Wavelength scale measured	3.97 - 4.01 μm
Temperature range	200 - 500 °C
Integration time	87 μm
Type of detector	Indium

Table 7: Characteristics and parameters IR camera for pre-heating tests.

Thermal resolution	20 mK at 30 °C
Frequency	150 Hz
Type sensor	50 mm
Numerical resolution	320 x 256 pixels
Estimated spatial resolution	4.7 mm/pixel
Wavelength scale measured	3.97 - 4.01 μm
Temperature range	5 - 300 °C
Integration time	22 μm
Type of detector	Indium

High speed camera

The optical device consists of a Photron SA1 camera, coupled to a Titanar objective. The other specifications are listed in Tab. 8

Table 8: Characteristics and parameters HSC camera.

Frequency	1000 Hz
Focal length	100 mm
Spatial resolution	46.5 pixel/mm